Open Archive Toulouse Archive Ouverte (OATAO)

OATAO is an open access repository that collects the work of Toulouse researchers and makes it freely available over the web where possible.

Influence of Yb:YAG Laser Beam Parameters on Haynes 188 Weld Fusion Zone Microstructure and Mechanical Properties

JÉRÉMIE GRANEIX, JEAN-DENIS BEGUIN, JOËL ALEXIS, and TALAL MASRI

The weldability of 1.2 mm thick Haynes 188 alloy sheets by a disk Yb:YAG laser welding was examined. Butt joints were made, and the influence of parameters such as power, size, and shape of the spot, welding speed, and gas flow has been investigated. Based on an iconographic correlation approach, optimum process parameters were determined. Depending on the distribution of the power density (circular or annular), acceptable welds were obtained. Powers greater than 1700 W, welding speeds higher than 3.8 m mm^{-1}, and spot sizes between 160 and 320 μm were needed in the circular (small fiber) configuration. By comparison, the annular (large fiber) configuration required a power as high as 2500 W, and a welding speed less than 3.8 m min^{-1}. The mechanical properties of the welds depended on their shape and microstructure, which in turn depended on the welding conditions. The content of carbides, the proportion of areas consisting of cellular and dendritic substructures, and the size of these substructures were used to explain the welded joint mechanical properties.

I. INTRODUCTION

LASER welding, in particular with a CO_2 source, has been widely developed for many applications, because of its many advantages, such as low heat input, small heat-affected zone (HAZ), low distortion rate, and high welding speed.[1–3] Welding of metals, such as superalloys, with a YAG laser beam has still not been adopted in industry due to thermal management issues leading to low-energy laser beams.[4,5] However, these technological problems have been solved with the emergence of new disk sources that achieve higher power levels of 9 kW with excellent optical quality.[6,7] These new sources present many other benefits: thin disk lasers provide a higher level of reliability; lower electrical power supplies are needed; and larger Rayleigh ranges are achieved.[8] Furthermore, Nd:YAG or Yb:YAG lasers can be delivered *via* optical fibers, opening up a large field of 3D applications of robotic cutting or welding.

Different types of cracks and HAZ liquation can occur in weldments of superalloys: hot cracking,[9]

liquation cracking,[10] and cracking after annealing treatment. To improve their weldability, superalloys must have a small grain microstructure[11] and not be pre-weld heat treated,[12] and their total content of aluminum and titanium must be less than 6 wt pct.[13] A small number of works on laser welding of Haynes 188 alloy have been published. Odabasi *et al*.[14] analyzed the geometries of CO_2 laser welds as a function of the energy implementation. They showed that the width of the welds and more generally the fusion zone (FZ) volume increased with the amount of energy used. Yilbas *et al*.[15] demonstrated a fine dendritic structure at the center of the FZ, including a few marked HAZ. This result was also obtained by Caiazzo *et al*.[16] for dissimilar welding of Haynes 188—Inconel 718 by a laser process. They estimated the thickness of the HAZ to be approximately 20 μm. Odabasi *et al*. observed by optical microscopy no HAZ or cracks at the interface of the base material (BM) with the FZ, but noted a gradient in hardness between these two zones over several hundred microns. Electron probe micro analysis (EPMA) measurements performed by Makino *et al*.[17] showed that the FZ composition was identical to that of the BM after laser welding. There was thus no loss of chemical elements by spraying. Odabasi *et al*. calculated a partition coefficient, noted k, for the major chemical elements; this partition coefficient was close to 1. They also showed that the tendency to segregation was low in the CO_2 welding of Haynes 188 alloy.

Makino *et al*. were also interested in the mechanical properties of welded joints obtained by TIG and CO_2

JÉRÉMIE GRANEIX, JEAN-DENIS BEGUIN, and TALAL MASRI are with the LGP/ENIT/INPT, Université de Toulouse, 47 av. d'Azereix, BP1629, 65016 Tarbes Cedex, France, Contact e-mail: Joel.alexis@enit.frmailto JOËL ALEXIS is with the LGP/ENIT/INPT, Université de Toulouse, and also with the Laboratoire Génie de Production, Ecole Nationale d'Ingénieurs de Tarbes, 47 avenue d'Azereix, BP1629, 65016 Tarbes Cedex, France.

laser welding of Haynes 188 alloy sheets.[17] For the whole temperature range of measurement during the mechanical tests, the yield strength of the welds was almost the same as that of the parent metal. The maximum strength and ductility were 95 and 60 pct of those of the parent metal, respectively. It should be noted that welds made by laser have a better resistance than TIG welds, but a lower ductility. The failure modes of TIG and laser specimens were comparable, and the rupture occurred at the center of the molten zone. Odabasi *et al.* furthermore showed that the beads mechanical properties were inferior to those of the parent material.[14] These mechanical properties deteriorated with increasing energy used, which was attributed by the authors to an increase in the interdendritic spacing. The fracture of welded samples was described as ductile. It started at tungsten- and lanthanum-rich precipitates, and spread between dendrites. Yilbas *et al.* studied by finite element simulation the evolution of the thermal gradient and mechanical stresses generated during laser welding of Haynes 188 alloy sheets.[15] During heating, mechanical stresses are low because of low stiffness values at high temperatures. In contrast, from the first moments of cooling, mechanical stresses can reach high values in areas of high temperature gradients.

In the present study, Yb:YAG laser welding of Haynes 188 alloy sheets was carried out. Optimal welding parameters were identified. The microstructure and mechanical properties of these optimized welds were characterized. The fusion zone shape and final solidification structure of this alloy were evaluated as a function of the laser parameters.

II. EXPERIMENTAL METHODS

A cobalt-base Haynes superalloy 188 sheet of 1.2 mm thickness and with an average grain size about 70 μm (#4.5, ASTM E112 standards) was used as a base material. The sheet was solution annealed at 1448 K (1175 °C) for 1 hour, and this was followed by water quenching. The alloy chemical composition was determined using an optical emission spectrometer (Foundry-Master Xpert, Oxford), and found to be (in wt pct) 23.9 Ni, 22.1 Cr, 14.1 W, 2.02 Fe, 0.09 C, 0.79 Mn, 0.30 Si, and the rest Co. The samples were cut and butt-welded by a TRUMPF TruLaser Cell 3000 machine. The laser beam was a Yb:YAG TruDisk with a maximum continuous-wave power of 3.3 kW, and equipped with a special optical fiber comprising a 100 μm core fiber and a 400 μm coaxial fiber. A circular and an annular cross-section of the laser beam may be obtained at the focal point using the 100 μm core fiber and 400 μm coaxial fiber, respectively. The use of either fiber configuration provided an adjustment range of the focal diameter from 110 to 370 μm for the core fiber, and 450 to 750 μm (outer diameter of the core) for the coaxial fiber. Focal diameters between 370 and 450 μm were therefore inaccessible. For the 400 μm coaxial fiber, the inner diameter remained relatively constant for a fixed spot size and variable power values. On the other

hand, it gradually increased from 200 to 314 μm as the diameter of the spot increased from 500 to 750 μm. Hereafter, the acronyms SFC and LFC (for small and large fiber configurations) will be used to refer to the 100 and 400 μm fiber configurations, respectively.

A PowerMonitor™ was used to measure the power output of the Yb:YAG laser source. A FocusMonitor™, made by PRIMES, was used to achieve the beam caustic specified in the standard ISO 11146 2005.

The samples were cut perpendicularly to the weld line for the microstructural characterization, while they were mechanically polished and then etched with a 96 pct HCl + 4 pct H_2O_2 solution for 2 seconds for the optical and scanning electron microscope (SEM) observations, and the electron backscatter diffraction (EBSD) analysis. Mechanical polishing was performed according to the following procedure: after a surface grinding with a 40 μm grain SiC paper, the specimens were polished with diamond pastes of 3, 1, and 0.25 μm granulations for a few minutes each. The microstructure was observed under an optical microscope and a scanning electron microscopy-field emission gun (SEM-FEG) microscope (JEOL 7000F). All EBSD analyses were performed using a SEM equipped with a phosphor screen and a charge-coupled device (CCD) camera (OXFORD Nordlys Fast camera). A 0.5 μm step size was used for scanning the samples. The EBSD data were then post-processed using the commercial orientation imaging software package Oxford Channel 5. To minimize measurement errors, all grains comprising less than 3 pixels were automatically removed from the maps prior to data analysis. To determine the microstructure of the Haynes 188 alloys and welds more precisely, in particular to elucidate the nature of the precipitates, diffraction analyses were performed at the European Synchrotron Radiation Facility (ESRF). All the analyses were carried out on beamline ID15 with a wavelength of 0.0142222 nm. Eight calibration tests were conducted with four beam sizes and two sample-detector distances on a CeO_2 powder ($a = 0.541165 \pm 0.0000059$ nm, crystallite size $= 380 \pm 4.5$ nm without micro stress). Varying the sample-detector distance was used to improve the precision of the lattice parameter measurements, while a smaller beam size was used to increase the number of diffraction peaks at the expense of accuracy. All values were calculated on the peak corresponding to the (311) plane of the fluorite structure of the CeO_2 powder.

Tensile tests were performed on the Haynes 188 alloy and welds using a DEBEN 5 kN machine with a strain rate of 1.1×10^{-3} s^{-1}. The results were compared with those determined for the reference alloy. The local mechanical behavior of different welds was furthermore analyzed by an image correlation method during the tensile tests using a camera system coupled to the 2M ARAMIS software (GOM).

To identify the influential parameters of the welding process while at the same time streamlining testing, an experimental design was established using the CORICO software.[18] The CORICO method is based on an analysis of partial correlations between all the variables of the experimental design.[19] The CORICO software calculates correlations between factor and responses,
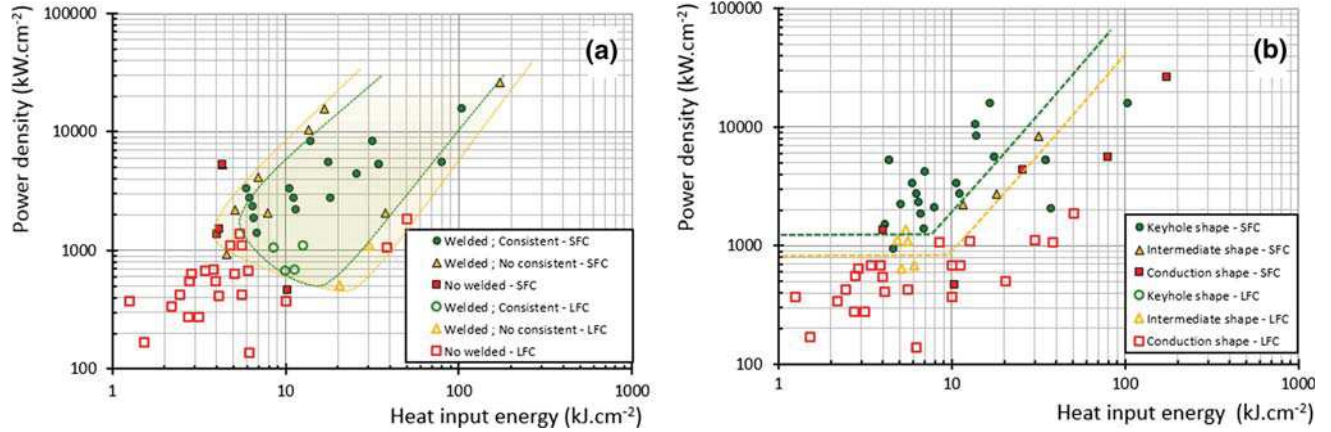
Fig. 1—(a) Domain of weldability of 1.2 mm thick sheets of alloy Haynes 188. (b) Areas of power density and input heat energy values yielding similar weld shapes of Haynes 188.

Table I. Parameter Values for Optimized Welds According to Criteria Based on the Standard ISO 11146 2005

	SFC	LFC
Laser power (W)	2097	2353
Welding velocity (m min^{-1})	4.12	1.39
Focused beam diameter on the surface (μm)	370	750
Shielding gas flow rate (L min^{-1})	33	40

and retains only significant correlations. Four parameters were selected for this study: the laser power (500 to 2500 W), speed welding (1 to 8 m min^{-1}), the focal diameter (110 to 750 μm) and the gas flow. The position of the focal point relative to the surface of the sheet was not investigated, as a previous study of the laser beam showed its minor role in view of the very large Rayleigh length.

III. RESULTS AND DISCUSSION

A. *Domain of Weldability of Haynes 188*

Dimensional limits for specific common imperfections in laser beam fusion welding are provided in the referred specifications EN ISO 6947; in particular, square joints in butt configurations need to be checked in terms of their reinforcement, low weld, drop-thru, underfill, undercut, and shrinkage groove. To validate the weldability of these alloys, the dimensions of the weld section were measured and compared to those given in the standard specifications EN ISO 6947. The domain of weldability of the Haynes 188 alloy as a function of the input heat energy and power density is shown in Figure 1(a). Welds complying with the standard specifications were obtained for a power density greater than 10^3 kW cm^{-2}, an input heat energy higher than 6 kJ cm^{-2}, and a power density/input heat energy ratio greater than 100. Macroscopic observations of the weld cross-section allowed us to distinguish three shapes of weld according to its width/height ratio (Figure 1(b)).

The weld shape was found to depend on the welding mode. Welds made in SFC generally had a keyhole shape, characteristic of the keyhole mode. The power density in SFC was always greater than 10^3 kW cm^{-2}, which is the minimum power density required for the formation of a capillary metal vapor,[20] allowing the keyhole mode. In this mode, a narrow, deeply penetrating vapor cavity, or keyhole, is formed due to local vaporization. The keyhole is surrounded by a thin layer of molten material which is maintained by an equilibrium between vapor pressure, surface tension, and hydrostatic pressure. The material at the leading edge melts and flows around the keyhole, solidifying to form a deep, narrow weld seam. On the other hand, the power density in LFC measured at the focal position never exceeded 2.10^3 kW cm^{-2}, which makes the keyhole mode impossible. The welds obtained in LFC had indeed the characteristic shape of welds made in the conduction mode.

This study was completed by the establishment of regression models based on process parameters to determine the optimal welding parameters. The execution of the multiple regression program under CORICO yielded logical interaction-based models. The optimization took into account all the geometric criteria specified in the standard EN ISO 11146 2005 and the mechanical properties of the welds. We considered as optimal welding parameters those which minimized the size of defects (low weld, drop-thru, underfill, undercut, and shrinkage groove) while maximizing the width of the weld, gas shield, and mechanical properties (ultimate tensile strain and elongation at rupture).[18] The corresponding optimal welding parameters are given in Table I.

B. *Microstructure of Optimized Welds*

In an attempt to establish a link between the process parameters, and the shape and size of the fusion zone, data such as the focal diameter and power density distribution were displayed on a same figure alongside the macrographs of the welds (Figure 2). For the welds obtained in the keyhole mode (SFC), the width of the
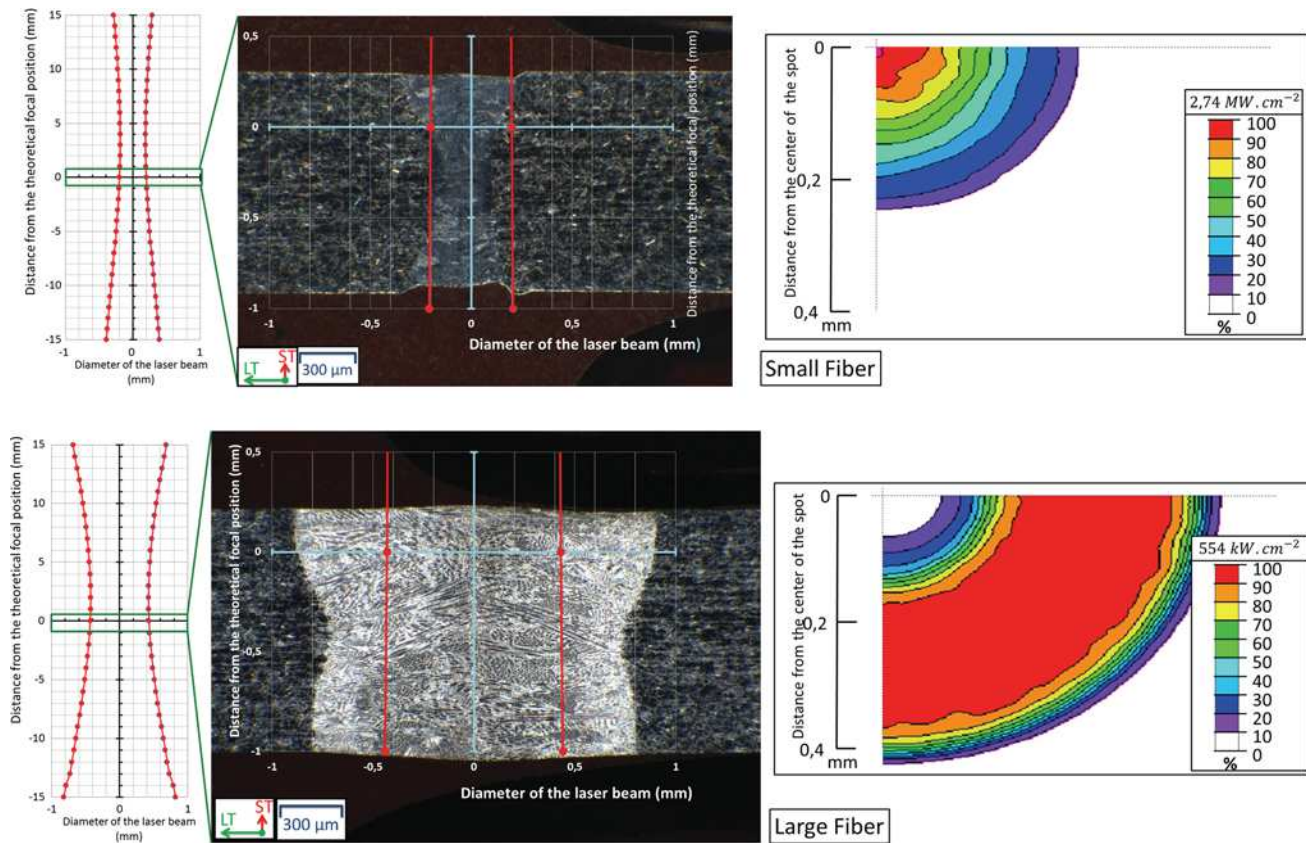
Fig. 2— Beam caustic, weld macrograph, and distribution of the laser beam power density in optimized conditions for both fiber configurations.

bead was determined by the laser beam diameter at the focal point. The phenomena of conduction and convection were minimal in this case. If the power density is less than that required to create a capillary and the welding speed is low, conduction and convection modes are promoted with the LFC fiber. The bead width was then greater than the maximum diameter at the focal point.

Micrographic observations of the bond line between the fusion zone and the parent metal showed no intergranular cracking in LFC (Figure 3). However, some grain boundaries were embossed on the surface, which points to a liquation phenomenon due to the generation of a HAZ during laser welding. This phenomenon did not cause any grain-coarsening phenomenon.

The different solidification substructures (cellular or dendritic) were determined for each optimized weld from many observations by optical and scanning electron microscopy at magnifications higher than ×500. Both dendritic and cellular zones are highlighted in the welds shown in Figure 4. As shown by some authors,[21,22] cellular substructures are located close to the weld-parent metal interface, while dendritic substructures are dominant in the center of the welds.

The secondary dendrite arm spacing in the center of the fusion zone was found to be larger in LFC welds (4.9 ± 0.6 μm) than in SFC welds (2.2 ± 0.2 μm). The secondary arm spacing increased with welding energy (Figure 5).[23]

Adabasi et al. found a similar positive correlation between the secondary dendritic arm spacing and the welding energy for Haynes 188 alloy.[14] The difference between Odabasi et al.'s results and those of this study may be due to the fact that Odabasi et al. used CO_2 laser welding, and a CO_2 laser beam has a wavelength ten times greater than that of a Yb:YAG laser beam. Additionally, their sheet thickness was 2.1 mm, i.e., thicker than that of this study. The energy input to the surface of the sheet was therefore less important in their study.

EBSD analyses were performed on cross-sections (LT-ST plane) and longitudinal-sections (RD-LT plane). Figure 6 shows an inverse pole figure of Z_0 mappings in the LT-ST plane of welds obtained in optimized LFC and SFC. The columnar grains grew from the parent metal to the center of the fusion zone, creating an interface at the center. Texture measurements were taken at the center of the welds and close to the BM (areas A and B). The intensity of the poles of the {100} planes family was greater in the center of the fusion zone (area B) than near the parent metal (area A). This difference in intensity was particularly obvious for the welds obtained in LFC. This can be explained by the selection of well-oriented grains during solidification. Furthermore, the columnar grains in the fusion zone were finer in the welds made in SFC. They tended to be smaller close to the parent metal and larger toward the center of the fusion zone. This grain size expansion is due to preferred growing conditions,
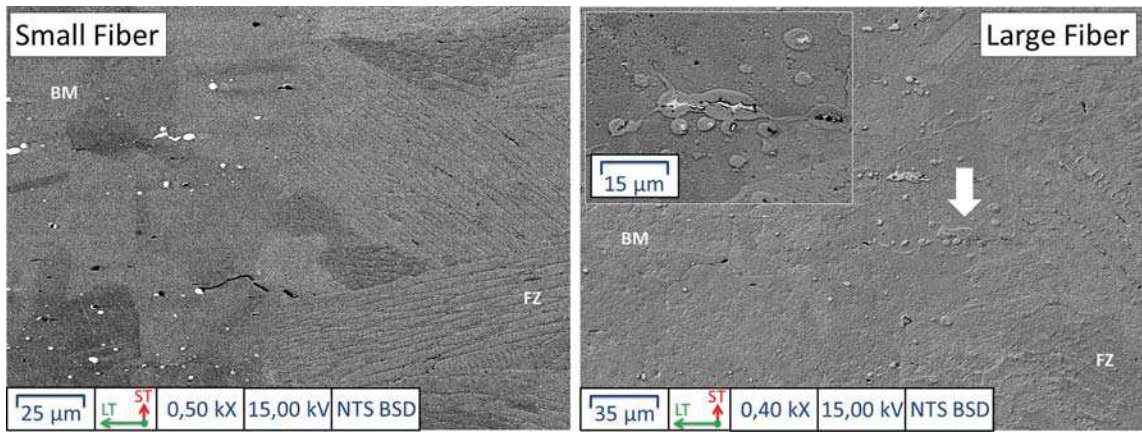
Fig. 3— SEM micrographs (backscattered electron mode) of optimized welds.
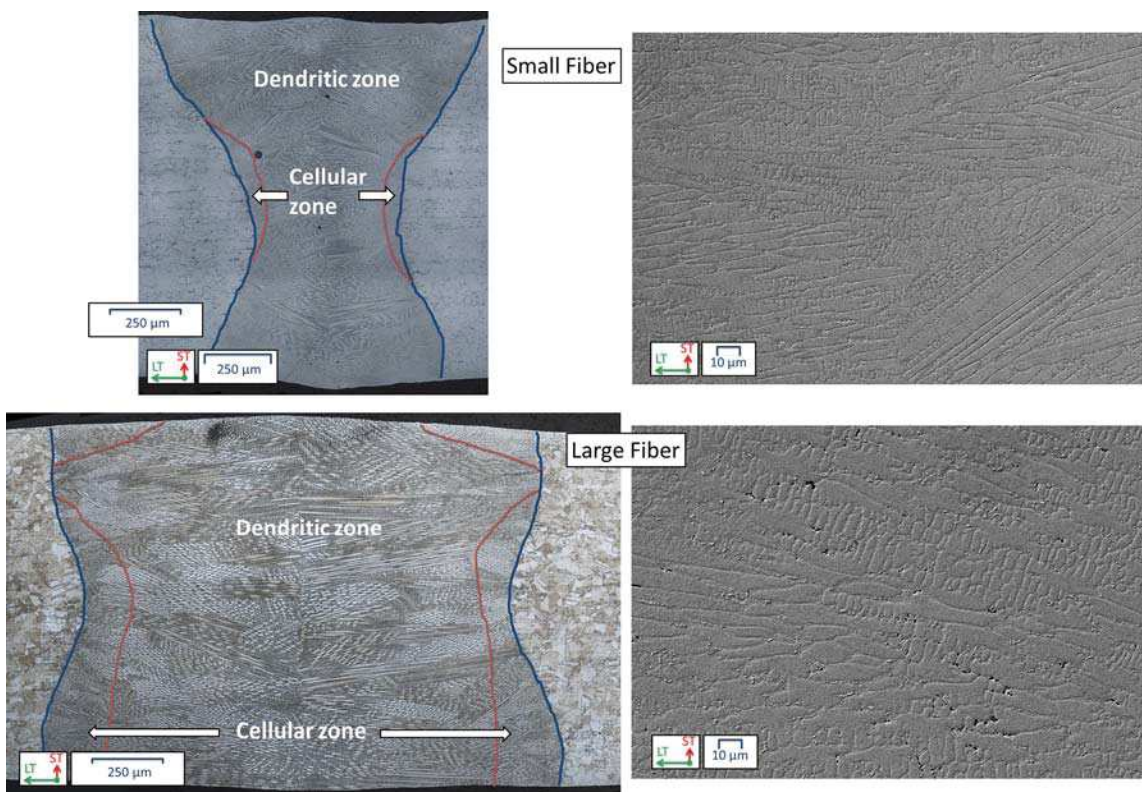

Fig. 4— Dendritic and cellular zones in the welds determined from optical observations at high magnification. SEM micrographs of the center of the welds.

and it causes the columnar grain crystallographic direction ⟨100⟩ to align with the heat flow direction. The microstructure in the fusion zone during solidification thus depended strongly on the microstructure of the parent metal and the welding conditions. The parent metal acted as a substrate on which columnar grains grew epitaxially.

EBSD additional observations were made in the RD-LT plane at the center of the sheet (Figure 7). They show that the grains grew perpendicularly to the solidification front at the center of the weld in view of the high welding speed.

The density of carbides in the weld compared to that in the parent metal was determined by X-ray diffraction. The analyses were performed in the RD-LT plane and included all types of weld beads (FZ, HAZ, BM). Each measurement point corresponds to a volume of sample analyzed in transmission over the whole thickness of the sheet. Two consecutive points were spaced by 100 μm. Figure 8 shows the ratio of the diffraction intensity by
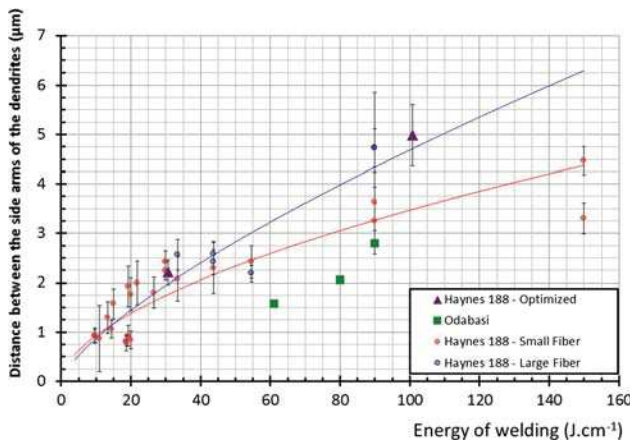
Fig. 5— Dendrite side arm spacing as a function of the welding energy.

the (422) planes of M_6C precipitates with respect to the diffraction intensity by the same planes in the parent metal for welded joints made in LFC and SFC, respectively. This figure provides information on the density of this type of precipitate in the different zones of the welded joint. Given that some welded joints were "keyhole shape" or "conduction shape," some analytical points corresponded to several zones (BM, HAZ, FZ). To interpret these data at best, the location of each measurement point is highlighted on each profile. The intensity ratio was much smaller in the fusion zone, but remained non-zero in both welding configurations. A precipitate gradient was observed between the BM and FZ for the welds obtained in LFC, while no such gradient was visible for the welds obtained in SFC. Note that the decrease in the intensity ratio towards the center of the weld obtained in SFC is also attributable to changes in the analyzed volume ratio (V_{weld} / V_{BM}).
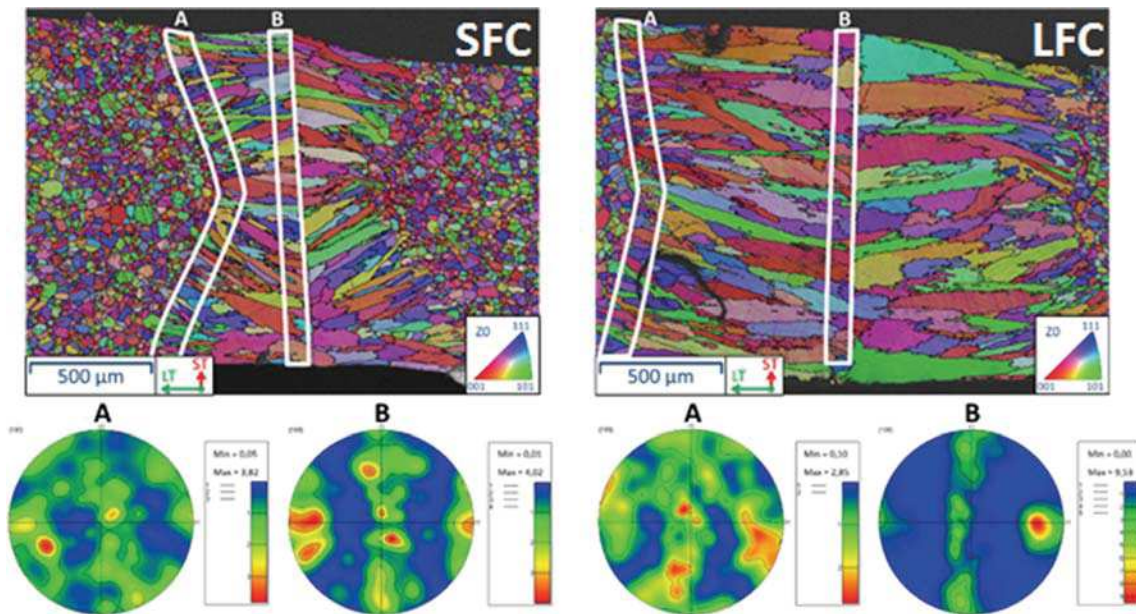

Fig. 6— EBSD inverse pole figure (IPF) Z_0 maps in the LT-ST plane of optimized welds (top). Texture intensity measured in areas A and B (bottom).
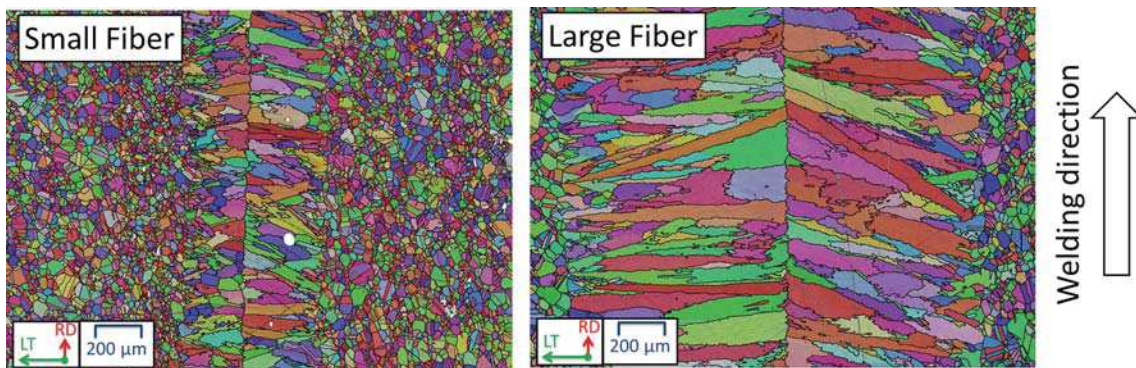

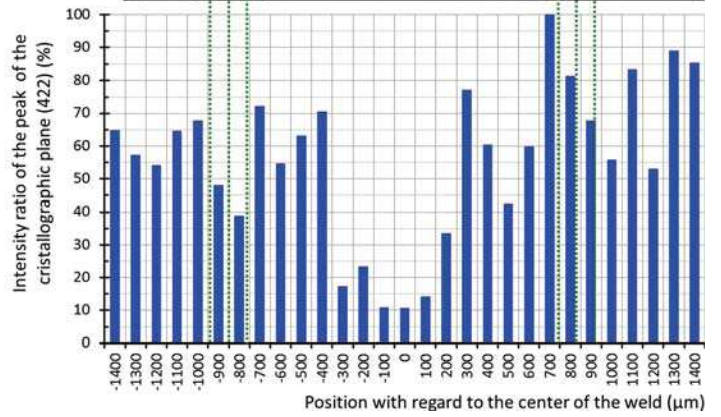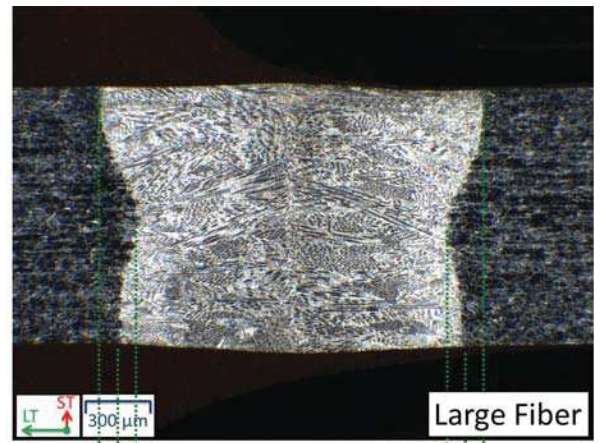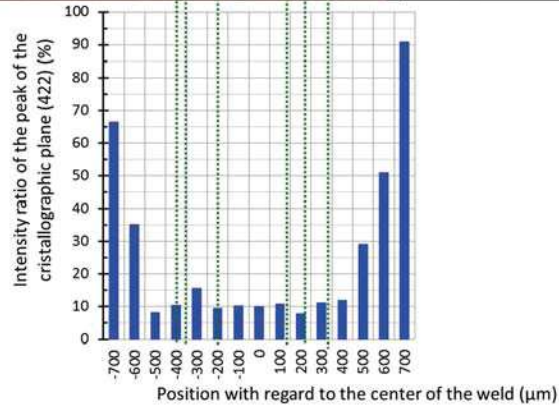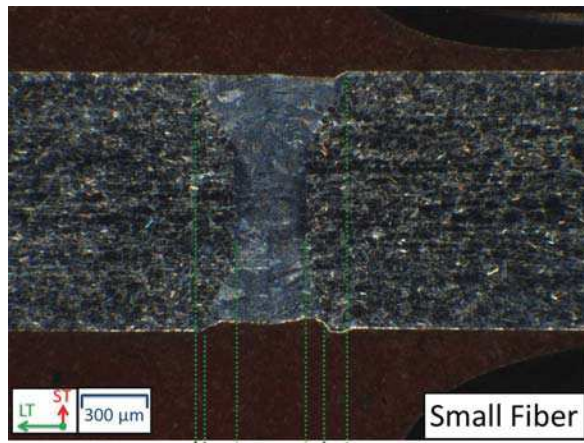Fig. 7— EBSD inverse pole figure Z_0 maps in the RD-LT plane of optimized welds.

Fig. 8— Location of the X-ray diffraction analysis of Haynes 188 welds obtained in SFC and LFC, respectively (top). Diffraction intensity ratio by the (422) planes of M_6C precipitates in the weld with respect to the base metal.
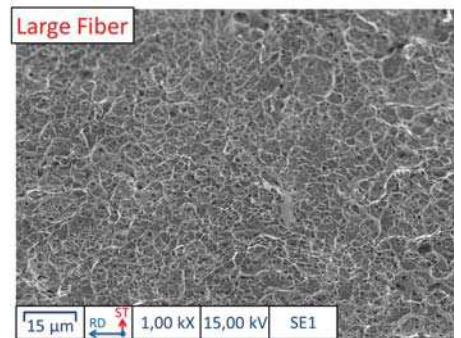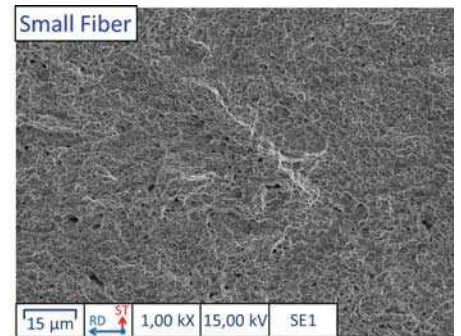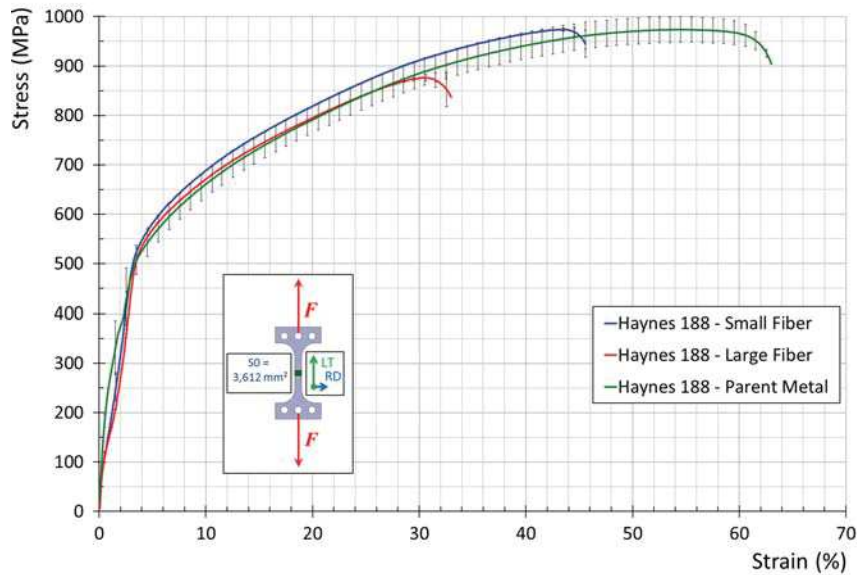

Fig. 9— Tensile curves along the direction transverse to the optimized weld obtained either in SFC or LFC. SEM images of the SFC (top) and LFC (bottom) weld fracture surface.

| Direction of Solicitation	Sample	Ultimate Tensile Strength (MPa)	Elongation (Pct)	Zone of Rupture
Transverse direction	SFC	975 ± 4	39 ± 0.1	fusion zone
Transverse direction	LFC	879 ± 11	27 ± 0.4	fusion zone
Longitudinal direction	SFC	917 ± 9	32 ± 0.9	fusion zone
Longitudinal direction	LFC	850 ± 10	35 ± 3	fusion zone
Rolling direction	parent metal	974 ± 37	57 ± 1.7	—
Long transverse direction	parent metal	997 ± 12	55 ± 1	—
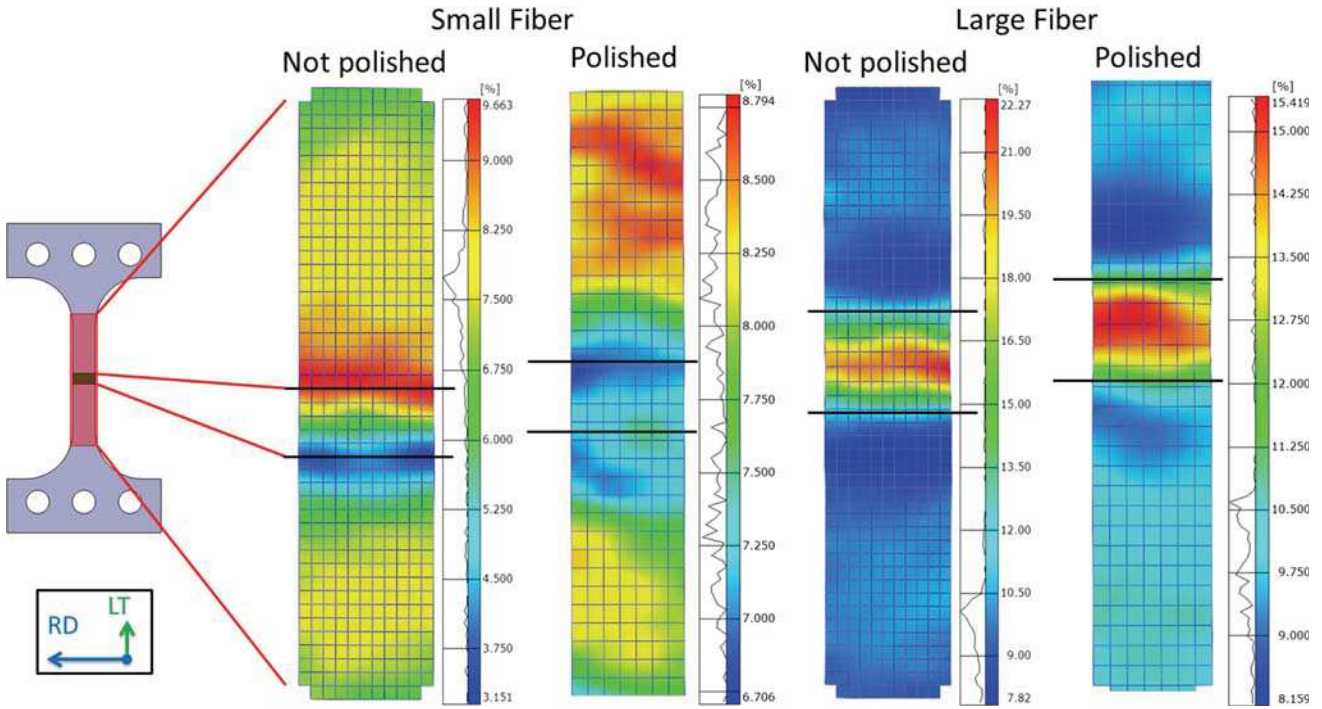
Fig. 10— Comparison of deformation fields in welds at a stress of 750 MPa before and after polishing.

C. Mechanical Properties of Optimized Welds

The stress-strain curves measured along the transverse direction to the weld seam of Haynes 188 are shown in Figure 9. They are very similar to that of the parent material also shown in Figure 9. The mechanical properties of welds differed mainly according to the type of fiber configuration, with a larger mechanical strength obtained with SFC samples and comparable to that of the reference alloy. The mechanical properties of the welded samples are given in Table II. By contrast to the mechanical strength, the ductility of SFC samples remained substantially lower. SEM observations of fracture surfaces also indicate a ductile failure, as well as the presence of dimples whose size depended on the fiber configuration. The SEM observations of the fractured samples showed that LFC welded samples had larger dimples. The better tensile properties observed for SFC samples with respect to LFC samples can be attributed in part to smaller dendritic spacings.

The local deformation fields in the welds were determined by digital image correlation (Figure 10).

For the SFC welds, polishing reduced the deformation gradient induced by gutters at the edge of the weld. The FZ deformed less than the BM. This result is however to be taken with caution given the small difference in deformation levels between the two zones. By contrast, we observed a significant deformation in the fusion zone of the LFC weld, regardless of the topography of the weld. This suggests different mechanical properties of SFC and LFC welds.

The study of the local mechanical properties of the weld seams was complemented by tensile tests along the welding direction on samples cut out with a laser around the weld seam. Given the welds geometry, the microstructure of the specimens may be heterogeneous and thus contain some parent metal. Both sides of the active area were polished with a grain size of 1200 (ANSI Grit size) to remove any effect of the topography of the weld. The tensile curves are shown in Figure 11. The maximum tensile strength of the fusion zone given in Table II is only 9 pct smaller than that of the Haynes 188 alloy, while the ductility values of the
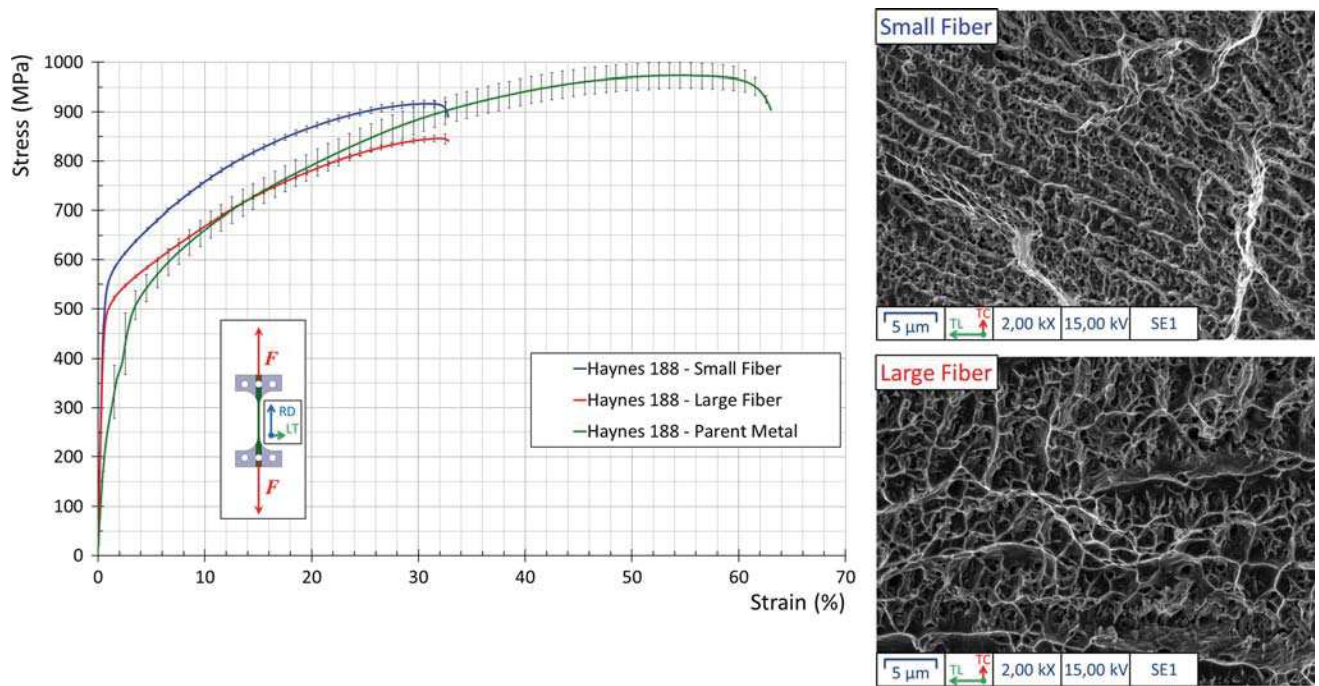
Fig. 11— Tensile tests performed on optimized weld beads. The mechanical stress was applied along the welding direction.

melted regions were reduced by a factor of nearly two. The fracture surfaces of the test pieces were observed by SEM and are shown in Figure 11. The fractography of tensile specimens showed a ductile fracture with the presence of dimples of the same size as those already observed on the fracture surface of welded joints subjected to stress in the transverse direction to the weld. In addition, an interdendritic fracture was observed.

The mechanical strength of the SFC welds in the transverse and longitudinal directions was greater than that of the LFC welds. Microstructural differences between these welds were found in terms of the content of carbides, proportion of cellular and dendritic substructures, and the size of these substructures. These differences could explain the different mechanical properties of the two types of welds.

IV. CONCLUSIONS

Three laser welding parameters (power of the laser source, welding speed and diameter of the laser beam at the focal point) were determined to ensure optimal weldability of the Haynes 188 alloy in agreement with EN ISO 13919. The minimum energy required for welding was reached very quickly in SFC due to the small beam diameter at the focal spot. The power should therefore not be excessive in SFC to avoid the risk of a collapse of the bath; the welding speed and the focal diameter, on the contrary, must be very high. Conversely, welding in LFC implied a smaller heat input energy, which in turn required a higher laser power and a reduced welding speed.

From multiple regression models, optimum parameters were calculated according to given geometric criteria. Similar welds realized in SFC were obtained in the keyhole mode, while LFC welds were obtained mainly in the conduction mode. Cell growth was observed near the parent metal, while dendrites were found at the center of the weld. The proportions of these different zones depended on the type of weld and thus on the welding conditions.

REFERENCES

1. W.W. Duley: *Laser Welding*, Wiley, New York, 1998.
2. W.M. Steen and J. Mazumder: *Laser Material Processing*, Springer, London, 2010 , pp. 199–249.
3. X. Gao, L. Zhang, J. Liu, and J. Zhang: *Mater. Sci. Eng., A*, 2013, vol. 559, pp. 14–21.
4. A.J. Kemp, G.J. Valentine, and D. Burns: *Prog. Quantum Electron.*, 2004, vol. 28, pp. 305–44.
5. N.P. Barnes: *IEEE J. Sel. Top. Quantum Electron.*, 2007, vols. 13–3, pp. 435–47.
6. A. Geisen and J. Speiser: *IEEE J. Sel. Top. Quantum Electron.*, 2007, vols. 13–3, pp. 598–609.
7. S. Ruppik, F. Becker, F. Grundmann, W. Rath, and U. Hefter: Proc. SPIE8235 Solid State Lasers XXI—Technology and Devices, 2012, vol. 8235, pp. 1–15.
8. T. Scheller, A. Bastick, and M. Griebel: Proc. SPIE 8239, High Power Laser Materials Processing: Lasers, Beam Delivery, Diagnostics, and Applications, 82390B, San Francisco, 2012, vol. 8239, pp. 1–10.

9. O.A. Idowu, O.A. Ojo, and M.C. Chaturvedi: Mater. Sci. Eng., A, vol. 454–455, pp. 389–97.
10. M. Pang, G. Yu, H.-H. Wang, and C.-Y. Zheng: *J. Mater. Process. Technol.*, 2008, vol. 207, pp. 271–75.
11. R.G. Thompson, J.J. Cassimus, D.E. Mayo, and J.R. Dobbs: *Weld. J.*, 1985, vol. 64 (4), pp. S91–96.
12. J.J. Pepe and W.F. Savage : *Weld. J. Res. Suppl.*, 1967, vol. 46 (9), pp. 411 22.
13. M. Zhong, H. Sun, W. Liu, and X. Zhuand : *J. He: Scr. Mater.*, 2005, vol. 53 (2), pp. 159 64.
14. A. Odabası, N. Ünlü, G. Göller, E. Kayalı, and M. Eruslu: *Mater. Sci. Eng., A*, 2013, vol. 559, pp. 731–41.
15. B.S. Yilbas and S. Akthar: *Int. J. Adv. Manuf. Technol.*, 2011, vol. 56 (1), pp. 115–24.
16. F. Caiazzo, V. Alfieri, V. Sergi, A. Schipani, and S. Cinque: *Int. J. Adv. Manuf. Technol.*, 2013, vol. 68 (5), pp. 1809–20.
17. Y. Makino, K. Honda, and S. Kimura: *Weld. Int.*, 1999, vol. 13, pp. 612–20.
18. J. Graneix, J.-D. Beguin, F. Pardheillan, J. Alexis, and T. Masri: *MATEC Web Conf.*, 2014, vol. 14 (13006), pp. 1–6.
19. M. Lesty: *La revue de Modulad*, 1999, vol. 22, pp. 41–77.
20. S. Postma. Weld Pool Control in Nd:YAG Laser Welding, thesis, Enschede, the Netherlands. Printed by Océ, 2003.
21. J. Brooks. Weld solidification and microstructural development trends in welding research. Proceeding of the 4th International Conference, 2003. pp. 123–133, Gatlinburg, Tennessee.
22. A.F. Giamei, E.H. Kraft, and F.D. Lemkey. New trends in Materials Processing: papers presented at a seminar of the American Society for Metals, October 19 and 20, 1974, Metal Parks, Ohio, 1976.
23. A.-M. El-Batahgy: *Mater. Lett.*, 1997, vol. 32, pp. 155–63.